



Metal ion activation and DNA recognition by the *Deinococcus radiodurans* manganese sensor DR2539

Cristiano Mota^{1,2,3} , Myles Webster¹, Melissa Saidi¹, Ulrike Kapp¹, Chloe Zubieta⁴, Gabriele Giachin⁵, José Antonio Manso^{6,7} and Daniele de Sanctis¹ 

¹ ESRF – The European Synchrotron, Grenoble, France

² Associate Laboratory i4HB – Institute for Health and Bioeconomy, NOVA School of Science and Technology, Universidade NOVA de Lisboa, Caparica, Portugal

³ UCIBIO, Applied Molecular Biosciences Unit, Department of Chemistry, NOVA School of Science and Technology, Universidade NOVA de Lisboa, Caparica, Portugal

⁴ IRTSV/LPCV, CEA, Grenoble, France

⁵ Department of Chemical Sciences, University of Padua, Italy

⁶ IBMC – Instituto de Biologia Molecular e Celular, Universidade do Porto, Portugal

⁷ I3S – Instituto de Investigação e Inovação em Saúde, Universidade do Porto, Portugal

Keywords

Deinococcus radiodurans; DtxR family; manganese homeostasis; metal regulator; protein-DNA complex

Correspondence

D. de Sanctis, ESRF – The European Synchrotron, 38000 Grenoble, France
 Tel: +33476882869
 E-mail: daniele.de_sanctis@esrf.fr

(Received 15 February 2024, revised 14 March 2024, accepted 10 April 2024)

doi:10.1111/febs.17140

The accumulation of manganese ions is crucial for scavenging reactive oxygen species and protecting the proteome of *Deinococcus radiodurans* (*Dr*). However, metal homeostasis still needs to be tightly regulated to avoid toxicity. DR2539, a dimeric transcription regulator, plays a key role in *Dr* manganese homeostasis. Despite comprising three well-conserved domains – a DNA-binding domain, a dimerisation domain, and an ancillary domain – the mechanisms underlying both, metal ion activation and DNA recognition remain elusive. In this study, we present biophysical analyses and the structure of the dimerisation and DNA-binding domains of DR2539 in its holo-form and in complex with the 21 base pair pseudo-palindromic repeat of the *dr1709* promoter region, shedding light on these activation and recognition mechanisms. The dimer presents eight manganese binding sites that induce structural conformations essential for DNA binding. The analysis of the protein-DNA interfaces elucidates the significance of Tyr59 and helix $\alpha 3$ sequence in the interaction with the DNA. Finally, the structure in solution as determined by small-angle X-ray scattering experiments and supported by AlphaFold modeling provides a model illustrating the conformational changes induced upon metal binding.

Abbreviations

AD, ancillary domain; *BhMntR*, *Bacillus halodurans* manganese transport regulator; *BsMntR*, *Bacillus subtilis* manganese transport regulator; CD, circular dichroism; *CdDtxR*, *Corynebacterium diphtheriae* diphtheria toxin regulator; DBD, DNA-binding domain; DD, dimerisation domain; DR, *Deinococcus radiodurans*; DTT, dithiothreitol; DtxR, diphtheria toxin regulator; EDTA, ethylenediaminetetraacetic acid; EMSA, electrophoretic mobility assays; ESI-TOF, electrospray ionisation time-of-flight; ITC, isothermal calorimetry; *MtIdeR*, *Mycobacterium tuberculosis* iron-dependent regulator; *MtMntR*, *Mycobacterium tuberculosis* manganese transport regulator; PDB, Protein Data Bank; ROS, reactive oxygen species; SAD, single wavelength anomalous diffraction; *SalMntR*, *Streptococcus gordonii* manganese transporter regulator; SAXS, small-angle X-ray scattering; *SelDeR*, *Sachararopolyspora erythraea* iron-dependent regulator; *SeSirR*, *Staphylococcus epidermidis* staphylococcal iron regulator repressor; *SgScaR*, *Streptococcus gordonii* streptococcal coaggregation regulator; *SmSloR*, *Streptococcus mutans* Streptococcal Lral family operon regulator; *SpMtsR*, *Streptococcus pyrogenes* multimetal transport system regulator; *TalDeR*, *Thermoplasma acidophilum* iron-dependent regulator; *TpTroR*, *Treponema pallidum* transport-related operon regulator; Tris, tris(hydroxymethyl)aminomethane.

Introduction

Deinococcus radiodurans (*Dr*) is a gram-positive bacterium highly resistant to stress conditions [1]. Since its discovery in 1956 [2], the molecular basis of its resistance has been the subject of several studies. While distinctive features such as multiple copies of its genome [3] and an efficient DNA repair system capable of restoring the entire genome through homologous recombination have been identified [4–7], these characteristics alone do not explain the resistance of an organism to environmental challenges. Beyond this, *Dr* presents a unique ability to protect its proteome against oxidative damage induced by reactive oxygen species (ROS). This exceptional trait enables *Dr* proteins to remain fully functional after exposure to stress conditions and facilitates the recovery and repair of bacterial DNA [8,9].

Dr presents higher ROS scavenging capacity when compared with other bacteria [10,11]. The scavenging is mediated by enzymatic (e.g. catalases, superoxide dismutases, and peroxidases) and non-enzymatic (e.g. divalent manganese complexes and carotenoids) components. Among these, manganese ions complexed with phosphates, nucleotides and amino acids emerged as the most powerful ROS scavengers in this bacterium [11]. The cellular concentration of these ions in *Dr* is higher compared with other bacteria, in contrast with relatively low iron levels [8]. However, if the high content of manganese benefits ROS scavenging, an excess of this divalent ion is still toxic to the bacteria and the manganese/iron homeostasis needs to be strictly regulated. Within the *Dr* genome, three types of manganese-dependent transport genes have been annotated: *dr1236* (encoding a manganese efflux protein) [12], *dr1709* (encoding an Nramp family transporter) [13–15], and the genes encoding ATP-dependent transporters (*dr2283*, *dr2284* and *dr2523*) [14,16,17]. On the other hand, the genes, which are implicated in iron-dependent transport, encode two ABC-type transporters (*drb0016*, *drb0017*), two Fe(II) transporters (*dr1219*, *dr1120*) and two DNA protection proteins (Dps) (*dr2263*, *drb0092*) [18]. The regulation of these transport systems is managed by three oxidation-related regulators, OxyR (DR0615) [19], the Ferric uptake regulator (Fur) homologue, DR0865 [20] and DR2539 [16,17]. DR0615 acts as both a transcriptional repressor of the *dps* and *mntH* genes and as an activator of the *katE* and *drb0125* genes. The Fur homologue, DR0865, is a positive regulator of *dr1236* efflux manganese transporter and a negative regulator of *dr2283*, *dr2284* and *dr2523* transporters [20]. DR2539 is reported to be a down-regulator of

manganese transporter genes (*dr1709* and *dr2283*) and an up-regulator of iron-dependent transporter genes (*dr1219* and *drb0125*) [17]. DR1709 is a member of the divalent metal transporters Nramp (natural-associated macrophage protein) family [15]. Nramp transporters have been identified in a wide range of organisms, from bacteria to humans, transporting iron in eukaryotes, while among prokaryotes, it demonstrates a preference for manganese transport [21–26]. This manganese transporter has been revealed to be essential for *Dr* growth [14] and one of the key proteins governing the remarkable manganese/iron homeostasis in the bacterium. Due to its regulatory role in *dr1709*, DR2539 has been proposed as the principal regulator of intracellular manganese homeostasis in *Dr* [16]. The diphtheria toxin regulator (DtxR) family, to which DR2539 belongs, was initially described with *Corynebacterium diphtheriae* DtxR (CdDtxR) as an iron-responsive repressor [27]. Later, extensive sequencing of bacterial genomes has revealed the details of multiple DtxR-like repressors, including IdeR from *Mycobacterium tuberculosis* (MtIdeR) [28,29], *Thermoplasma acidophilum* (TaIdeR) [30] and *Sachararopolyspora erythraea* (SeIdeR) [31], ScaR from *Streptococcus gordonii* (SgScar) [32], MntR from *Staphylococcus aureus* (SaMntR) *Bacillus subtilis* (BsMntR), *Bacillus halodurans* (BhMntR) and *M. tuberculosis* (MtMntR) [33–38], TroR from *Treponema pallidum* (TpTroR) [39], MtsR from *Streptococcus pyogenes* (SpMtsR) [40,41], SirR from *Staphylococcus epidermidis* (SeSirR) [42], and SloR from *Streptococcus mutans* (SmSloR) [43–45]. Several structures of CdDtxR homologues have been solved, revealing a modular domain organisation including an N-terminal DNA-binding domain (DBD), a dimerisation domain (DD) and a C-terminal domain, the ancillary domain (AD). Notably, the AD is missing in some MntRs. The molecular mechanisms of metal- and DNA-binding were already proposed by several authors [46–48], but structural differences and the variation in the number of metal-binding sites suggest different types of regulation among the different homologues [32].

In this study, we performed biochemical and biophysical studies to characterise the DR2539 regulator. We solved the crystal structures of the DNA binding and dimerisation domains in the holo-form, and in complex with the *dr1709* promoter region with its physiological cofactor (manganese). In addition to the primary and ancillary metal-binding sites, observed in other DtxR regulators, DR2539 reveals a novel metal

centre. Furthermore, SAXS studies, supported by the predicted model, contributed additional insights into the metal-induced conformational changes, the ancillary domain, and the full-length arrangement. These structures provide insights into the metal sensing and DNA-binding mechanisms of this key regulator of manganese/iron homeostasis in *Dr*.

Results

DR2539 expression and purification

The recombinant DR2539 protein was overexpressed and purified in two species that corresponded to the full length (25 kDa) and a cleaved stable form with 16 kDa molecular weight. Both species were well-separated using heparin affinity column purification (Fig. S1) and confirmed by N-terminal sequencing and by mass spectrometry (ESI-TOF), indicating that the protein suffered proteolysis in the C-terminus before the first purification step.

Overall structure of truncated DR2539 in the holo-form

The crystal structure of truncated DR2539 (DR2539tr, residues 4–142) was determined by SAD phasing using a dataset collected at 2.5 Å resolution at the wavelength of 1.771 Å. DR2539 crystallised in the $P4_32_12$ space group with unit cell dimensions $a = b = 60.8$ Å, $c = 187.7$ Å. The anomalous signal from Cd, present in the crystallisation buffer, allowed to locate a total of 17 anomalous peaks that were used to calculate the experimental phases. The refined model (R_{work} and R_{free} values of 20.5% and 25.5%, Table 1, PDB: 8PVT) was used for molecular replacement to solve the structure of a “native” dataset, collected at 2.0 Å resolution at the wavelength of 0.979 Å, which was eventually refined to crystallographic R_{work} and R_{free} values of 18.6% and 22.0%, respectively, with good geometry. This refined model (PDB: 8PVZ) contains 271 amino acid residues from two monomers in the asymmetric unit. The biological dimer is obtained by a symmetric operation and presents approximate dimensions of $65.7 \times 46.6 \times 35.5$ Å (Fig. 1). Each subunit is divided into three domains, a N-terminal DNA-binding domain (DBD, residues 4–64), a dimerisation domain (DD, residues 65–127) and a coil region (residues 128–141) that links the missing ancillary domain (Fig. 1 and Fig. S2). The DBD comprises three α -helices and a region that corresponds to a pair of antiparallel β -strands forming a hairpin, constituting a winged helix-turn-helix (HTH) motif. The region corresponding to the wing, antiparallel β -strands, appears

to be highly flexible, as evidenced by the higher B -factors. In one of the protomers, this region could not be fully modelled. The DBD and the DD are connected via $\alpha 4$ (residues 65–91) linking the DNA recognition domain to $\alpha 5$ and $\alpha 6$ helices from the DD. The solvent-accessible surface buried at the interface between the DD domains of the two monomers is 840.7 Å^2 ($\sim 11\%$ of the surface area), with 21 amino acid residues participating in the interface (PDBePISA protein–protein interaction server; http://www.ebi.ac.uk/msd-srv/prot_int/). The dimeric interface is mainly constituted by a hydrophobic patch composed by Leu82, Phe85, Leu86, Ala89, Leu90, Val92, Pro93, Ala103, Leu104, Ala107, Leu108, Leu112, Ile116 and Trp119 side chains, and by a network of 13 hydrogen bonds between and 11 salt bridges (Table S1). Gel filtration profiles of DR2539 incubated with manganese ions or in presence of EDTA yielded a single peak without significant differences between the elution profiles (Fig. S3) suggesting that DR2539 exists as a functional dimer in solution either in the apo or holo-form.

Cadmium ions present in the crystallisation buffer were used to calculate the experimental phases and provided initial insights into DR2539 metal-binding sites. The cadmiums bound to the protein were confirmed in the anomalous difference map calculated from the high resolution “native” dataset, which presents 12 peaks higher than 10σ and four additional peaks at about 5σ . Although, 22 Cd^{2+} ions were modelled in the final model, only four metal-binding sites were refined with full occupancy, two for each monomer, with temperature B -factors of 34.1, 34.6, 33.1 and 35.2 Å^2 , for CD1, CD2, CD3 and CD4, respectively. These four ions are bound to the two ancillary sites present in the asymmetric unit (Fig. 1) and they form binuclear metal centres. Two other cadmium ions are bound to the two primary sites present in the asymmetric unit (CD5 and CD8) with occupancies refined to 0.82 and 0.83 and B -factor of 45.6 and 33.3 Å^2 , respectively. Additionally, a previously unreported binding site is observed between $\alpha 4$ and $\alpha 6$ with high occupancies of 0.89 and 0.92 and B -factor of 36.1 and 34.9 Å^2 , respectively for the two chains (CD7 and CD9) (Table S2). This putative new metal-binding site is hexacoordinated to Glu74OE1, His78NE2, Glu113OE1, a bidentate interaction to Glu110 and one water molecule. The remaining cadmium ions are solvent exposed and are coordinated by charged residues, His15NE2, Glu50OE2, His56NE2, His87NE2, Asp95OD2, Asp99OD1, and His125ND1 with partial occupancies (Table S2) which are lower than the other sites and are most likely due to the high concentration of cadmium in the crystallisation solution.

Table 1. Crystallographic data collection and refinement statistics. Values in parentheses are for the highest resolution shell. Friedel pairs were merged.

Structure	Cd-DR2539 (SAD)	Cd-DR2539 (MR)	Mn-DR2539- <i>dr1709p</i>
PDB ID	8PVT	8PVZ	8PW0
Data collection and processing			
Beamline	ID29 (ESRF)	ID23-1 (ESRF)	ID29 (ESRF)
Wavelength (Å)	1.771	0.979	0.976
Resolution (Å)	43.6–2.50 (2.64–2.50)	46.9–2.00 (2.11–2.00)	47.9–2.20 (2.32–2.20)
Space group	P4 ₃ 2 ₁ 2	P4 ₃ 2 ₁ 2	P4 ₃ 2 ₁ 2
Cell dimensions <i>a</i> , <i>b</i> , <i>c</i> (Å)	60.85, 60.85, 187.49	60.78, 60.78, 187.68	67.71, 67.71, 158.14
No. unique reflections	12 916 (1752)	24 727 (3534)	19 507 (2768)
<i>R</i> _{merge}	0.168 (1.014)	0.103 (1.221)	0.093 (1.016)
<i>R</i> _{meas}	0.187 (1.074)	0.113 (1.344)	0.099 (1.074)
<i>R</i> _{pim}	0.038 (0.256)	0.047 (0.555)	0.033 (0.339)
<i>I</i> / σ <i>I</i>	16.2 (2.8)	11.4 (2.2)	13.1 (1.9)
Completeness (%)	99.4 (96.3)	99.8 (99.9)	100.0 (100.0)
Multiplicity	23.2 (16.5)	5.5 (5.8)	8.8 (9.2)
CC1/2	0.998 (0.864)	0.998 (0.622)	0.998 (0.678)
Anomalous completeness (%)	99.6 (96.3)	97.3 (99.2)	99.98 (99.8)
Anomalous multiplicity	23.2 (16.5)	2.9 (2.9)	4.7 (4.8)
Refinement			
Resolution (Å)	43.6–2.5 (2.60–2.50)	43.6–2.00 (2.08–2.00)	47.88–2.20 (2.26–2.20)
No. of reflections	12 852	24 643	19 457
<i>R</i> _{work} / <i>R</i> _{free} (%) ^a	20.49/25.50	18.56/22.00	18.26/22.73
No. of non H-atoms			
Protein	2078	2093	1046
DNA	–	–	856
Metal ions	23	24	4
Water	57	139	92
<i>B</i> -factors			
Protein (Å ²)	40.00	41.00	58.23
DNA (Å ²)	–	–	50.96
Metal ions (Å ²)	77.66	55.78	81.11
R.m.s. deviations			
Bond lengths (Å)	0.004	0.013	0.008
Bond angles (Å)	0.706	1.185	1.095
Ramachandran favoured/poor (%) ^b	99.25/0.75	99.26/0.74	97.78/1.48
Rama Z-score ^b	–1.01	0.91	–0.38
Clash score ^b	6.96	3.57	3.20
Molprobity score ^b	1.67	1.28	1.36

^a*R*_{free} is calculated from a randomly selected subset of ~ 5% of reflections excluded from refinement; ^bGeometry statistics were calculated with MOLPROBITY [78].

Overall structure of DR2539tr-*dr1709p*-manganese complex

DR2539 specifically recognises the promoter region (ATTTTAGTCGCGCTAAAT) of its target gene (*dr1709*) and affects its transcription [16,17]. We obtained crystals of DR2539tr bound to the 21 bp promoter region of the manganese transporter *dr1709p* gene (*dr1709p*) and we solved the structure of the complex at 2.2 Å by molecular replacement using the structure of the holo-form (PDB: 8PVZ) as the search model. This structure, refined to crystallographic

*R*_{work} and *R*_{free} values of 18.3% and 22.7% (Table 1) contains one protein monomer of 136 amino acids and a 21-mer single strand DNA. Because the DNA sequence is quasi-palindromic (differing in 2 base pairs) the 21-mer double-stranded DNA was refined with 50% occupancy in the asymmetric unit with the biological dimer generated by a crystallographic two-fold axis (Fig. 2A). For this reason and because of the odd number of nucleotides there is ambiguity in three base pairs (forward Thy8, Cyt13, and Ade21, Fig. S4).

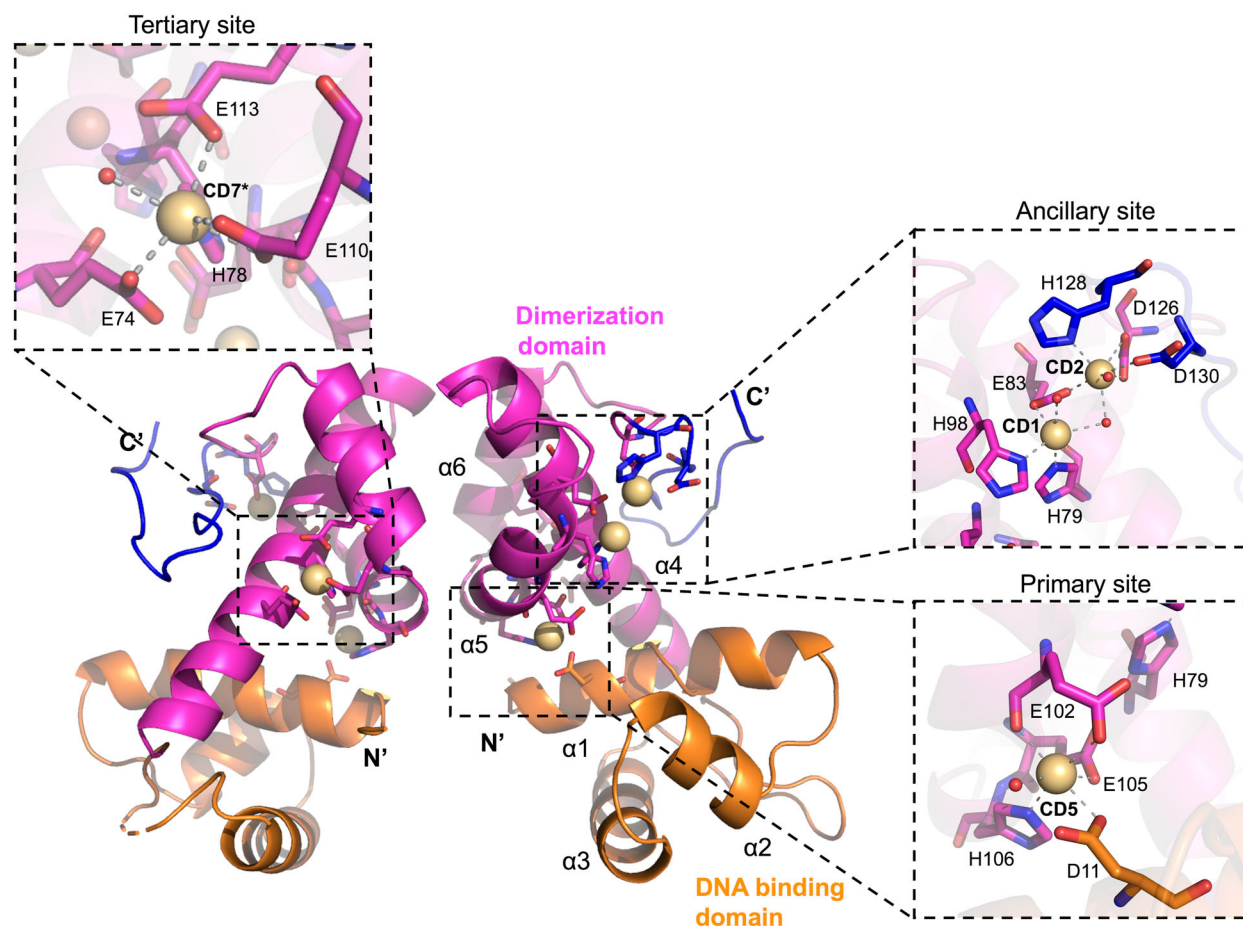


Fig. 1. The three-dimensional structure of holo truncated DR2539 (DR2539tr). The biological dimer, generated by a twofold crystallographic symmetry operation. Inset images show a close-up view of the primary, ancillary, and tertiary metal-binding sites. The DNA-binding domain is represented in orange, the dimerization domain in magenta, and the linker that would connect the missing C-terminal ancillary domain is shown in blue. Cadmium atoms are represented as spheres in wheat colour. Structure images were created with PYMOL [78].

The overall structure of DR2539tr in complex with DNA revealed moderate differences (r.m.s.d. of 1.34 Å) in comparison with free holo-protein, however the DNA-binding resulted in an increased distance of 3 Å between carbon- α of the α -helices 3 from both monomers (Fig. 2B). DR2539tr dimer binding to DNA B-form results in a slight bending of the DNA, with a total curvature angle of 3.9° (as calculated by CURVES+) [49] (Fig. 2A). In fact, the major groove in correspondence of Cyt9 to Gua12 and Thy15 to Ade17, is narrowed by approximately 2 Å compared to canonical B-DNA and accommodates the DNA-binding helices α 3 of the HTH motif. Consequently, the minor groove is widened by about 3 Å, and shallower than in a canonical B-form DNA (Fig. S5). Circular dichroism spectra titration measurements confirm the DNA bending also in solution, excluding crystallisation artefacts (Fig. S6).

DR2539 recognises the *dr1709* promoter region

The DR2539 recognises the *dr1709* promoter region in both full-length and truncated forms in presence of manganese (Fig. 2C). The region comprising helices α 2 and α 3 from the HTH motif (residues Ser26-Gln51) located in the DBD, is responsible for most of the DNA binding and recognition (Table S3). Each DBD recognises a characteristic 5-bases pairs DNA sequence that constitutes the major groove which nests helix α 3. However, only a few interactions are occurring in the residue range Ala37-Lys47 (Fig. 2D,E). Several non-specific polar interactions are observed between the DBD and the phosphates of the DNA backbone which are flanking both sides of the major groove. The side chains of Ser26, Thr27, Gln28, Thr42, Arg46, His56 are interacting with the 5'-3' forward strand and Ser40 and Lys47 with the reverse. The reverse strand

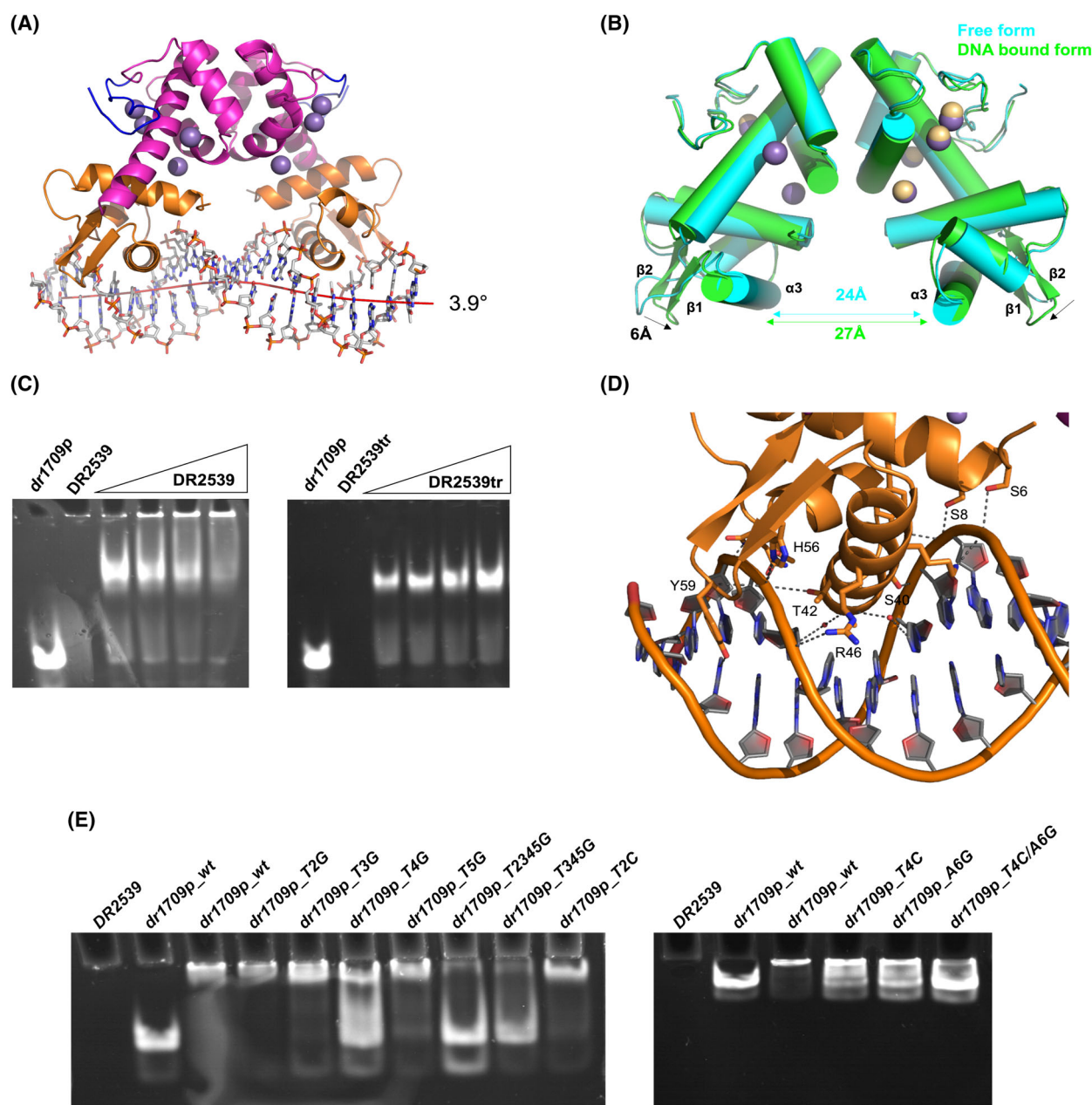


Fig. 2. DR2539tr-*dr1709p* interactions. (A) Structure of the biological dimer DR2539tr bound to *dr1709* promoter region (21 bp), the DNA curvature (red line) was calculated by CURVES+; (B) Superposition of DNA bound (green) and free (cyan) DR2539tr forms and relative distance between the DBDs. Manganese and cadmium as purple and wheat spheres, respectively. (C) EMSA analysis with PAGE of *dr1709p* (1 μ M) binding by titrating DR2539 (lanes 3–6: 5, 10, 15, 25 μ M). Negative controls with *dr1709p* and DR2539 are in lanes 1 and 2, respectively. DNA presence is revealed by SYBR green. On the left, full-length DR2539; on the right, truncated DR2539 (DR2539tr) was used. The non-migration of the band of DR2539 full length at concentrations above 10 μ M could be explained either by protein aggregation or formation of bigger complexes. (D) Representation of the interactions between one DR2539 monomer (DNA-binding domain, in orange) and the *dr1709* promoter region. Hydrogen bonds and salt bridges are indicated by dashed grey lines. (E) EMSA analysis on the effect of different mutations in the DNA recognition sequence (see Table S4). Left gel, from left to right: DR2539, *dr1709p_wt*, *dr1709p_wt* and DR2539, *dr1709p_T2G* and DR2539, *dr1709p_T3G* and DR2539, *dr1709p_T4G* and DR2539, *dr1709p_T5G* and DR2539, *dr1709p_T2345G* and DR2539, *dr1709p_T345G* and DR2539, *dr1709p_T2C* and DR2539; Right gel, from left to right: DR2539, *dr1709p_wt*, *dr1709p_wt* and DR2539, *dr1709p_T4C* and DR2539, *dr1709p_A6G* and DR2539, *dr1709p_T4C/A6G* and DR2539. The concentrations of DNA and DR2539 used were 1 and 5 μ M, respectively. EMSA assays were performed in triplicate. Structure images were created with PYMOL [78].

also establishes polar interactions with the N-terminal residues, Ser6, Ser8 and Tyr12 (Fig. 3). The turn Gly35-Ala39 interacts with nucleotide bases through

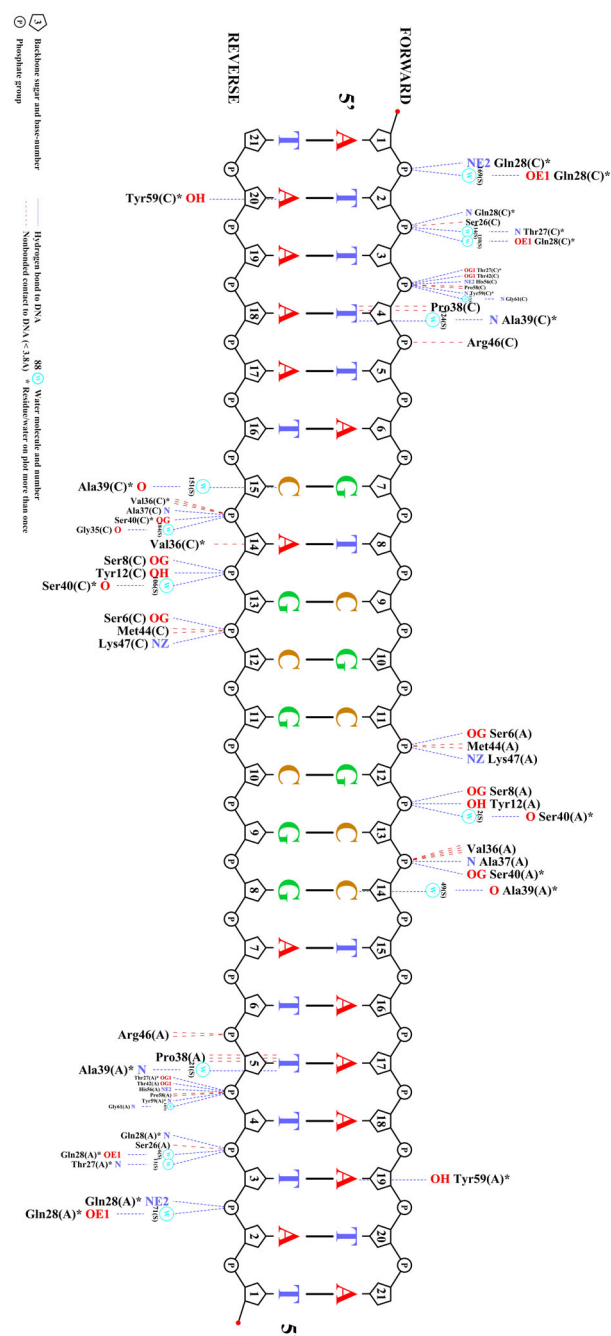


Fig. 3. Schematic representation of the specific interactions between DR2539 and *dr1709p*. Nucleotides bases are represented by one-letter codes and coloured according to their type. Hydrogen bonds are drawn as blue dashed lines and non-bonded contacts as red dashed lines. Atom names are coloured blue for nitrogen and red for oxygen. Water molecules are drawn as cyan circles and labelled by their PDB number. Figure generated by Nucplot [79].

hydrophobic interactions between Ala37 and Pro38 with C7 methionine groups from reverse thymine16 and forward thymine4, respectively. This interaction defines the specificity for the cognate DNA sequence. Additionally, Ala39 backbone forms hydrogen bonds with two water molecules, and these further interact with O4 from thymine 4 and N4 from reverse cytosine 15.

When with the free form, in the complex, the wings of the winged helix motif, β -strands β 1 and β 2 from both monomers, are 6 Å closer (distances measured between Tyr59 C α atoms), pinching the forward strand. Tyr59 is nested into the minor groove and establishes a specific hydrogen bond with the N3 atom from the reverse strand adenine 20 (Fig. 2D). Additional interactions are formed between the main chain and DNA mediated by water molecules (Fig. 3).

In order to assess the importance of the individual nucleotide bases at different positions, the binding of oligos presenting point mutations on the *dr1709* promoter region (Table S4) to DR2539 was evaluated by gel mobility shift assays (Fig. 2E). The hydrogen bond established by Tyr59 and the reverse adenine 20 and the hydrophobic interactions of helix 3 and the major groove were probed in this experiment. The results revealed the role of thymine 4 and reverse thymine16, in which their C7 methyl groups establish hydrophobic interactions with Pro38 and Ala37, respectively. In addition, these two nucleotides share some hydrogen bonded waters with the protein backbone. Mutation of these two nucleotides is enough to dramatically decrease DNA binding (Fig. 2E), highlighting the fact that those positions are critical for efficient DNA binding and specificity. We could observe that mutations that affected the hydrophobic interactions (thymine4 and reverse thymine16) were disruptive, while mutations on the reverse adenine 20 and, consequently, hydrogen bond break with the DR2539 wing amino acid, Tyr59, is not essential in the sequence recognition (Fig. 2E), but it rather suggests that the role is mainly in the stacking van der Waals interactions of the phenol ring that is nested in the DNA minor groove. Single mutations of forward thymines 3 and 5 showed no shift in the gel while mutation of all nucleotides in the major groove resulted in complete loss of binding (Fig. 2E).

DR2539 presents 4 manganese binding sites

We observed that DR2539 recognises the *dr1709* promoter region exclusively in the presence of divalent cations. EMSA assays suggest that DR2539tr has affinity for different metal ions, with a distinct

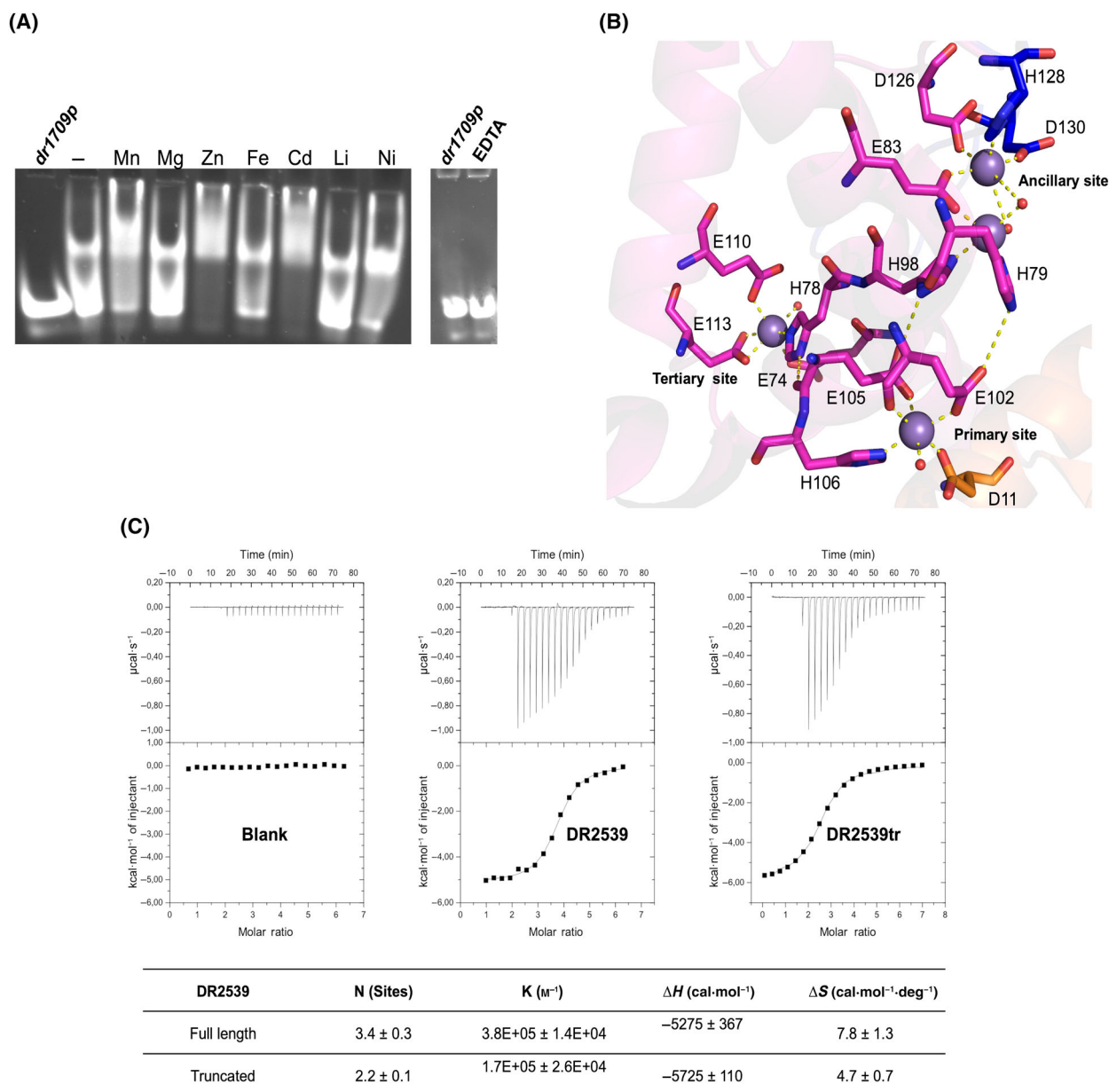


Fig. 4. DR2539 binding to metals. (A) EMSA analysis of DR2539tr (5 μM) binding to *dr1709p* (1 μM) when incubated with different metal ions (0.5 mM): left gel, lane 1: negative control with *dr1709p*, lanes 2–9: no metal added (–), manganese (Mn), magnesium (Mg), iron (Fe), cadmium (Cd), lithium (Li), nickel (Ni); right gel, lane 1: negative control with *dr1709p*, lane 2: incubation in the presence of EDTA. (B) The hydrogen bonds and coordination network (dashed yellow lines) of the manganese binding sites in one of the DR2539 monomers, manganese ions are shown in purple and water ligands are represented as small red spheres. (C) Calorimetric titration of DR2539 full-length and truncated forms at 50 μM with 20 injections of 2 μL from MnCl₂ at 1.5 mM, and below, the table of thermodynamic parameters calculated by Isothermal Titration Calorimetry (ITC). EMSA and ITC assays were performed in triplicate. Structure images were created with PYMOL [78].

preference for transition metals Mn²⁺, Zn²⁺, Fe²⁺, Cd²⁺ and Ni²⁺ (Fig. 4A). The negative control performed without metal supplementation (Fig. 4A), indicates that DR2539 can bind to *dr1709p* by uptake of metals either from the media or electrophoresis buffers, while in the presence of EDTA no binding is

observed (Fig. 4A). The same effect is observed when the DNA is titrated with DR2539 protein and monitored by Circular Dichroism in the 280 nm region (Fig. S6). Thus, metal binding is required for the recognition of *dr1709p* DNA sequence by DR2539, providing a direct mechanism connecting metal binding

by DR2539 to transcriptional outputs. Contrary to the previously determined structures from the DtxR family, that could bind up to a maximum of three metals [38,45], DR2539 presents four manganese binding sites in each monomer, the first metal-binding site we call the primary site (coordinated by Asp11OD1, Glu102OE2, Glu105OE2 and His106NE2), a binuclear ancillary site consisting of ancillary site I and, ancillary site II (coordinated by His79NE2, Glu83OE2, His98ND1, Asp126OD2, His128ND1 and Asp130OD2) and an additional site located in the dimerisation domain, here entitled “tertiary site” (coordinated by Glu74OE2, His78NE2, Glu110OE1 and OE2, and Glu113OE1) (Fig. 4B). These residues forming the new metal-binding site are not conserved in the DtxR family (Fig. S2), suggesting that this additional metal site is a peculiarity of DR2539, conserved in *Deinococcus* species [50]. The anomalous difference Fourier map shows strong peaks of 11σ , 9.3σ , 6.5σ and 10.5σ for primary, ancillary sites I and II and tertiary sites, respectively.

Although the incorporation of metals is essential for *in vitro* DR2539 binding to DNA [16], the role of each individual metal-binding site is still unclear. In order to further investigate metal binding, isothermal titration calorimetry (ITC) assays were performed on the full-length and truncated versions. The titration curve showed a sigmoidal shape that could be fitted to one set of sites binding model with 3.4 manganese ions ($K_d = 2.6 \mu\text{M}$) and 2.2 metals ($K_d = 5.8 \mu\text{M}$) for the full-length and the truncated forms, respectively, inferring that the C-terminal domain contributed to the formation of at least one of the binding sites (Fig. 4C). The presence of only one transition slope (although at different stoichiometric ratios, for the two forms) indicates that the dissociation constants for the different metal-binding sites are in the same order of magnitude.

Full-length DR2539 presents a compact conformation in solution

The ancillary domain appears to be non-essential for *in vitro* DNA binding, as both truncated and full-length protein presented a similar migration profile in the gel (Fig. 4A). Nevertheless, based on the elution profiles on heparin columns, DR2539 full-length and truncated species in presence of manganese ions suggest that they may exhibit different DNA-binding affinities, proposing that the ancillary domain might influence in some manner the DNA binding (Fig. S1). Additionally, the ancillary domain has also been associated with protein–protein interaction and the

formation of higher complexes, displaying a critical role *in vivo* [51].

Using AlphaFold2 (AF2) [52], a model for the full-length DR2539 (Fig. 5A and Fig. S7) was generated and further validated by SAXS experiments. In this model the AD contacts the DD and Asp163 is in position to coordinate the binuclear metal ancillary site (Fig. 5B). The position of the ancillary domain is variable in the different crystal structures of the DtxR family and the AD-DD interaction is proposed to be a step of the activation mechanism [47]. In order to probe the interactions of these domains, we performed SAXS experiments. SAXS data revealed that both DR2539 full-length and truncated forms are dimers in solution either in apo or holo-forms (Table S5), with the calculated Porod's volumes corresponding to the mass of the dimer. The analysis of the full-length form aimed to identify the position of the ancillary domain and its possible implication in metal regulation. However, the full-length protein was prone to aggregation, especially when incubated with manganese or EDTA (Fig. S8). Dilution series were performed to overcome this and the least aggregated samples were obtained for the as-isolated form and the measured scattering curves were analysed. The Guinier region of the scattering curve yields a radius of gyration of 28 \AA and analysis of the pair distribution function ($P(r)$) derived from the scattering curve obtained suggests a maximum intramolecular distance of 83 \AA . This is in agreement with the AF2 model since the theoretical scattering calculated for this model reproduces nearly the experimental data with a χ^2 of 2.9 (Fig. 5C). This model also docks into the ab initio molecular envelope (Fig. 5D), indicating that the ancillary domain is likely facing the dimerisation domain, allowing it to complete the ancillary metal-binding site, likely contributing with a bidentate coordination of Asp163. Furthermore, we wanted to evaluate the possible flexibility of the ancillary domain with respect to the rest of the protein. For that, an ensemble optimisation method (EOM) was employed. A pool of 10,000 DR2539 full-length structures was generated, assuming the ancillary domain fully flexible. The minimal ensemble that better fits the experimental data was mainly populated by a conformation with a narrower size distribution than the entire size range of the pool (Fig. 5E). This clearly indicates limited flexibility for the AD domain and supports a compacted model in which the ancillary domain should be close to the dimerisation domain in the as-isolated form.

As mentioned above, full-length protein was more prone to aggregate in the presence of additives (manganese or EDTA) which made it difficult to analyse

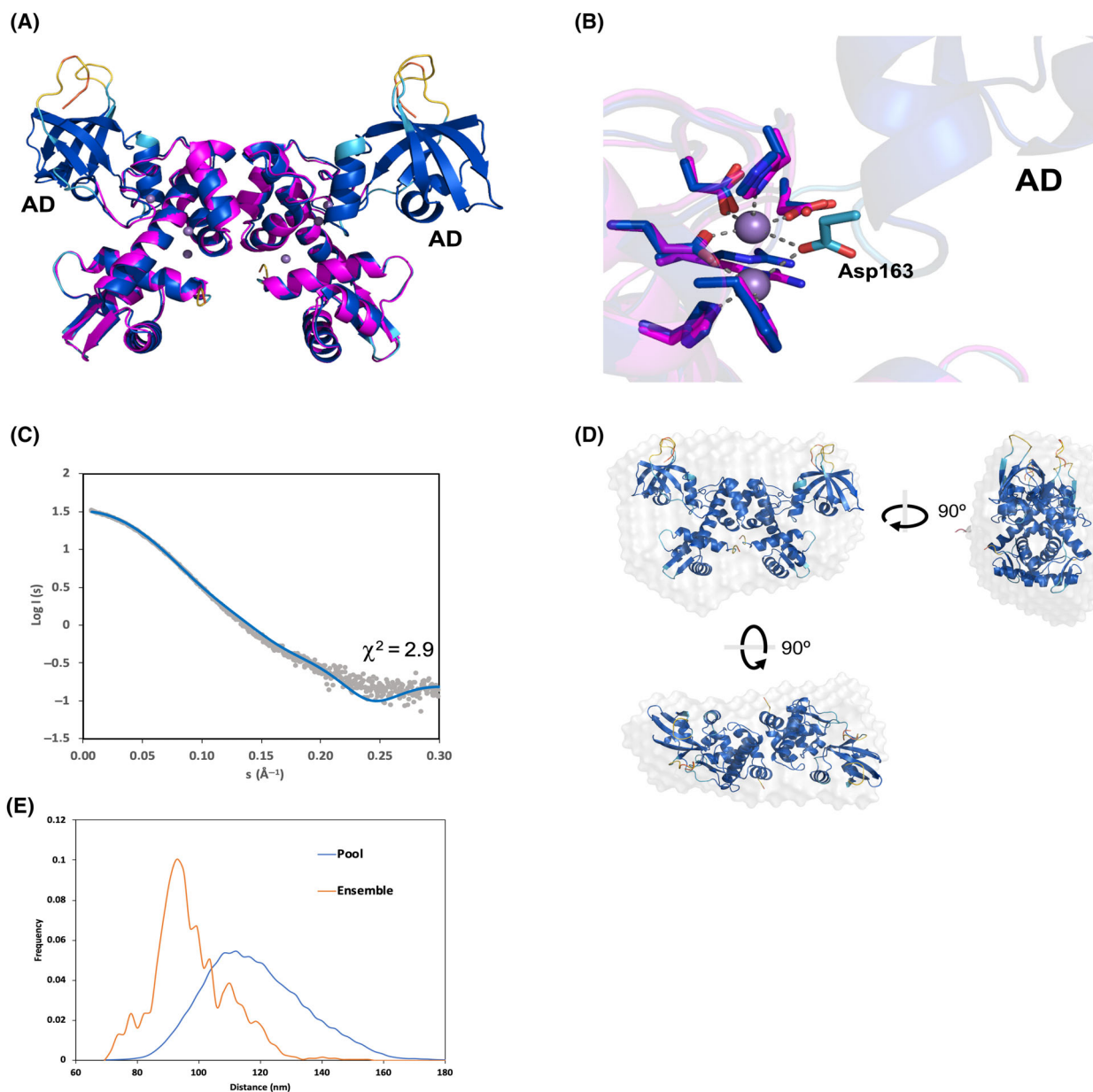


Fig. 5. DR2539 full length is a dimer in solution and displays compact arrangement. (A) AlphaFold2 model of full-length DR2539 coloured by confidence (pLDDT: dark blue > 90 very high confidence, cyan 90 > pLDDT > 70 confident, yellow 70 > pLDDT > 50 low; orange 50 > pLDDT very low) superposed with experimental structure (PDB: 8PW0, in magenta). (B) Close-up view of the AD-ancillary site interactions with the predicted AF2 model superposed. Manganese ions in purple. (C) Experimental Small-angle X-ray Scattering (SAXS) profile by merging 10 scattering curves obtained at low and high protein concentrations (grey dots) and calculated scattering (blue line) for the DR2539 dimer (model generated by AlphaFold2). (D) Ribbon representation of DR2539 model (generated by AF2) docked into the SAXS-derived molecular envelope (semi-transparent surface), generated by DAMMIF [76], which is the average of 15 independently reconstructed bead models. Three orthogonal views are shown. (E) Ensemble optimization method analysis of the flexibility between two rigid segments (DBD-DD and AD) comprising residues 1–126 and 146–233. Frequency distributions of the distances in a pool of models (blue line) and in the selected ensemble that fits the SAXS data of DR2539 (orange line).

SAXS data (Fig. S8). Nonetheless, aiming to study the effect of metal binding in the metal regulator activation, we also incubated the as-isolated truncated form

with manganese or EDTA. SAXS analysis of the protein solutions in the Guinier region shows a decrease of the R_g upon metal binding, from 27.8 Å in the

EDTA incubated sample to 24.6 Å in the manganese incubated sample (Table S5). These results suggest flexibility between DD and DBD and the compact form is achieved at least with insertion of the metal in the primary site. The experimental model (PDB: 8PVZ) fits better the data of the manganese incubated sample with a χ^2 of 5.7 (Fig. S9).

Discussion

The role of DR2539 in *Deinococcus radiodurans* and its structure

Metalloregulators play a pivotal role in maintaining the bacterial metal homeostasis by sensing the cellular metal abundance or shortage. This work highlights the structural and biophysical features of the manganese homeostasis regulator, DR2539, crucial in the cellular oxidation response of *Dr* [16]. The overall structure of DR2539 presents the three characteristic domains of the DtxR family: the N-terminal DBD, the dimerisation domain and the ancillary domain. The latter is absent in our crystal structure due to spontaneous proteolysis. Although the overall fold is conserved, this protein revealed unique features both in metal incorporation and in protein-DNA interactions that could be related to the uncommon Mn homeostasis of *Dr*. Unlike other reported members of the DtxR family, for which it was proposed that the metal cofactor binds to the monomer and consequently promoting conformational changes that induce the dimerisation, our study reveals dimerisation is not metal dependent, with no evidence for monomeric DR2539 in the absence of metals [46,47].

DR2539 metal-binding sites in comparison with other DtxR family members

DR2539 presents structural and functional differences from homologues. The structure of the ternary complex (DR2539tr:DNA:Mn) unveils four manganese binding sites. The primary binding site in DR2539 is constituted by acidic residues, characteristic of manganese-specific regulators, whereas iron-specific binding regulators present sulphur containing amino acids. Contrary to the *BsMntR* and *BhMntR* homologues, which present a binuclear centre, with a glutamate coordinating the second metal in a bidentate fashion, DR2539 presents Lys14 in this position, which impairs the formation of a binuclear centre in the DBD-DD interface. The presence of a positive charge is also observed in *CdDtxR* and *MtIdeR* with an arginine at this position. On the other hand, DR2539

presents a bimetal centre in the ancillary domain, which further contributes to anchoring this domain and modulating the activity of the repressor. The ancillary site, that in the case of *CdDtxR* and *MtIdeR* is a mononuclear centre and it is coordinated by two residues from the ancillary domain, in DR2539, *SmSloR*, *SgScar* and *MtMntR*, it is coordinated by only one residue from the AD, Asp163 (DR2539 numbering). Moreover, although the second metal is not directly coordinated to the AD, it aids the interaction between DD and AD. While in DR2539 this bimetal site is shaped by three histidines (His79, His98 and His128), three aspartates (Asp126, Asp130 and Asp163) and one Glu83, *SmSloR*, *SgScaR*, *SpMtsR* and *TaIdeR* present a cysteine replacing the first aspartate residue (Fig. S2). The presence of binuclear centres appears to be a peculiarity of Mn activated regulators from DtxR family, at the point that it has been suggested that the geometry of the binuclear centre serves to select manganese over other transition metals, which is likely the case, given the versatility of histidine in binding metals [53].

The new metal-binding site identified in the dimerisation domain, between helices $\alpha 4$ and $\alpha 6$, suggests a role in stabilising the interaction between the dimerisation and DNA-binding domains. The presence of a fourth metal in the tertiary site is confirmed by stoichiometric binding ratio of 3.4 manganese ions to the full-length protein (Fig. 4C) and it seems to be a peculiarity of DR2539. The four metal-binding sites are part of a hydrogen bonding network, suggesting that, despite the similar affinities, the metal incorporation is part of a step-by-step mechanism. In the holo-form, Glu102 hydrogen bonds to His98 and Glu105 to His79 (Fig. 2D). Furthermore, His78, coordinating the tertiary site, is only 3.8 Å from the backbone carbonyl of Glu105, which coordinates the primary site.

According to the proposed *CdDtxR* mechanism, the ancillary site is the highest affinity site, and the primary site is the low affinity site [47]. However, considering manganese anomalous signals in the ternary complex, we found that the primary and tertiary sites show higher anomalous differences, pointing to tighter binding compared to the ancillary sites. We should nevertheless consider the fact that the ancillary domain is missing, hence the corresponding metal-binding site could be loose due to the lack of the coordinating residue (Asp163). Furthermore, in solution, isothermal titration analysis showed that the truncated form loses one metal compared to the full-length protein. This result, supported by the full-length AlphaFold model, suggests that the ancillary domain may be involved in the coordination of the missing metal.

***dr1709p* sequence recognition by DR2539**

According to the mechanism proposed for *CdDtxR* [47,54], a multistep metal-binding induces conformational changes that promote protein-DNA interaction. The N-terminal amino acids Ser6, Ser8 and the conserved Tyr12 establish hydrogen bonds with DNA phosphate groups promoted by the conformation held by the primary metal site, while it presents a limited number of salt bridge interactions (only Arg46 and Lys47 from $\alpha 3$ helix) when compared with the structures of *MtIdeR* and *CdDtxR* in complex with DNA [55] that show an extended positively charged patch that interacts with the negatively charged phosphate backbone.

Helix $\alpha 3$, that is nested in the DNA major groove, reveals a close sequence similarity among groups of subfamilies: *CdDtxR*, *SeIdeR* and *MtIdeR*; *SgScaR*, *SmSloR*, and *SpMtsR*; DR2539 and *MtMntR*; and *TaIdeR* (Figs S2 and S10). In the first two subfamilies, the helix $\alpha 3$ first residue is a proline that participates in the interface with the DNA. In DR2539, the first residue of $\alpha 3$ is Ala39, which interacts directly with Thy5 of the forward filament and Thy16 of the reverse (Fig. 3). In this position a bulkier side chain would reshape the interface, likely diminishing the affinity for the DNA strand. *MtMntR* does not present any proline in the region, and the first residue is a serine suggesting a different protein-DNA interaction [38].

The fifth residue of helix $\alpha 3$ in the homologous proteins (Gly43 in DR2539, Fig. S2) has been reported [56,57] to interact directly by hydrogen bonding with the nucleotides of a G-C base pair and to recognise the correct DNA sequence [57]. While homologous proteins have a polar residue with long side chain, DR2539 presents instead Gly43, which permits to recognise and bind either binding boxes of *dr1709p*, and the variability in the DNA sequence in the position #8, that breaks the palindrome sequence.

DR2539 regulation mechanism

DR2539 is a dimer in the apo-form and is fully loaded with 8 manganese ions in the holo-form. Primary and ancillary sites are conserved from homologous proteins, but an additional metal-binding site in the dimerisation domain was observed for the first time, contributing to increase metal:protein activation ratio. The Mn concentration in the whole cell of *Dr* is approximately 200 μM , although free Mn ions are estimated at 2 μM [11]. This concentration aligns closely with the dissociation constants for DR2539 and Mn determined by ITC, 2.6–5.9 μM (Fig. 4).

The flexibility between DBD and DD suggested that metal-binding site 1 is critical to DR2539 scaffold and DNA recognition, with SAXS data supporting that manganese ion binding on the primary site is responsible for the stabilisation of the DBDs and the correct spacing between them. The DBD-DNA interaction presents unique features, differently from the N-terminal helix-to-coil transition induced by metal binding and DNA-induced conformational changes observed in *CdDtxR* [57,58]. In DR2539, the N-terminal residues are in the opposite direction compared to *CdDtxR*: DNA complex (PDB: 1C0W) and Ser6 establishes a hydrogen bond with O from phosphate of DNA backbone. Additionally, contrary to *CdDtxR*, the N-terminal is not making any interaction with the primary binding site. Binding of DNA to DR2539 holo-form triggered conformational changes of the DBD orientation, thereby favouring the interaction of certain residues with DNA (Fig. 3). The distance between the $\alpha 3$ recognition helices is increased to match the spacing between two consecutive major groove regions. Additionally, Tyr59 from the antiparallel β -sheet motifs, interacts with adenines 19 and 20 from the forward and reverse strands, respectively. Although the tyrosine may play a role in a latch closing mode which is usually occupied by charged residues in the homologous proteins, the perturbation of the hydrogen bond caused no visible effects in the “*in vitro*” qualitative binding experiments (Fig. 2E). On the other hand, the recognition of the major groove is essential with special attention to interactions to thymine 4 and reverse thymine 16 that are crucial in recognition, although single mutations do not completely impair “*in vitro*” DNA binding.

The role of the ancillary domain in DR2539

In *CdDtxR* and *MtIdeR*, the C-terminal domain is either coordinating the ancillary metal site and interacting with dimerisation and DNA binding domains or in variable positions, stabilised by crystallographic contacts [55,59]. Although several structures from the DtxR family lack electron density to model this domain due to the flexibility provided by the long linker, most of the DR2539 linker (Pro127-Pro140) is well defined in the electron density map of the truncated protein and forms a double hairpin, with the first turn involved in the formation of the ancillary metal-binding site. The long linker connecting the dimerisation and ancillary domains is compatible with an extended apo-form in solution, however the EOM analysis on the SAXS data excludes a high degree of flexibility of this region, suggesting that, in the as-isolated form, the AD is close to the DD in a compact form. Although, in absence of

metals, DR2539 presented a tendency to aggregate, potentially indicating an important change in protein globularity.

The structural comparison with *SgScaR*, *SmSloR* and *MtMntR* and the AlphaFold model reveals the presence of structurally conserved aspartate residues (Asp163 in DR2539) that participate in forming the ancillary metal-binding site and could contribute to structure the double metal-binding site, modulating the repressor activation in function of the metal ion concentration.

Additional sequence analysis identifies this domain as a member of the FeoA superfamily (pfam 04023). FeoA is a small cytoplasmic beta-barrel protein that presents a SH3-like fold (NMR structural studies of *Escherichia coli* FeoA, PDB: 2LX9). SH3-like domains are usually involved in protein–protein interactions [60]. Although protein oligomerisation through the C-terminal domain was proposed for the *SpMstR* and *SeIdeR* homologues [51,61], it is not consensual that this behaviour is common in the entire DtxR family. The amino acids proposed in protein–protein interactions (Y167 and F187 in *SpMstR* to T171 and A191 in DR2539, respectively) are not conserved in DR2539, however their chemical nature is conserved (Fig. S2), therefore, it cannot be excluded a similar oligomerisation behaviour in compatible conditions.

Although the ancillary domain is not essential for *in vitro* DNA binding, we observe some differences between full-length and truncated forms. The AD modulates the binding, probably through the metal incorporation into the ancillary metal-binding site, which stabilises the entire scaffold. These results agree with *CdDtxR* *in vivo* studies, showing that the absence of the ancillary domain leads to a less active repressor [54].

Conclusion

The current study elucidates the structural determinants of the metal regulator DR2539 in metal binding and DNA interaction. This regulator is revealed to be key in manganese homeostasis and consequently in ROS scavenging. DR2539 exhibits specificity for manganese binding enabling the transcription factor to bind DNA and activate or inactivate transcription of target genes, including the known manganese transporter *dr1709*. When compared to homologues, DR2539 presents the highest metal loading capacity, which, along with lower protein–*dr1709p* specific interactions, may contribute to enhancing concentration of manganese in *Dr*. The presence of the ancillary domain, while it is not essential for *in vitro* DNA regulation, shapes the binuclear ancillary metal-binding site, modulating the DNA binding. Although no higher oligomeric forms were observed in

this study, we cannot exclude that *in vivo* additional cofactors or higher oligomerisation states may be present due to assembly of multiple factors on the genomic DNA.

Materials and methods

Cloning, expression and purification

The gene encoding DR2539 protein was amplified by polymerase chain reaction using the genomic DNA of *D. radiodurans* as a template. It was inserted into the *EheI/HincIII*-digested expression vector pProEx HTb (Life Technologies, Carlsbad, CA, USA), resulting in a 25-residues hexahistidine-containing tag at the N-terminus. The recombinant DR2539 was expressed in *E. coli* BL21 (DE3) (Invitrogen, Waltham, MA, USA). The cells were grown at 310 K to an OD₆₀₀ of ≈ 0.6 in Luria-Bertani medium containing 100 $\mu\text{g}\cdot\text{mL}^{-1}$ of ampicillin. Protein expression was induced using 1 mM isopropyl β -D-1-thiogalactopyranoside (IPTG). Cell growth continued at 289 K for 14 h after IPTG induction and the cells were harvested by centrifugation at 7000 *g* for 20 min at 277 K.

The cell pellet was resuspended in lysis buffer (50 mM Tris–HCl pH 7.5, 1 M NaCl, 10% (v/v) glycerol, 2 mM β -mercaptoethanol, 1.5 M urea) to which DNase I was added to a final concentration of 20 $\mu\text{g}\cdot\text{mL}^{-1}$ together with an EDTA-free protease inhibitor tablet (Roche Applied Science, Penzberg, Germany). Cells were disrupted by three cycles of freeze/thaw and the suspension was then homogenised using an ultrasonic processor (QSonica, Newtown, CT, USA). The crude cell extract was centrifuged at 40 000 *g* for 45 min at 277 K. The supernatant was filtered in 0.45 μm filter and loaded into a 5 mL His-trap FF column (GE Healthcare, Chicago, IL, USA) pre-equilibrated with buffer A (50 mM Tris–HCl pH 7.5, 500 mM NaCl, 5% (v/v) glycerol, 1.5 M urea, 5 mM imidazole). The column was washed with buffer B (50 mM Tris–HCl pH 7.5, 500 mM NaCl, 5% (v/v) glycerol, 5 mM imidazole). A first washing step was performed with 10% buffer C (50 mM Tris–HCl pH 7.5, 500 mM NaCl, 5% (v/v) glycerol, 500 mM imidazole) followed by a gradient from 10% to 100% of buffer C, in 20 column volumes. The eluted fractions purity were evaluated by SDS/PAGE, with two forms of DR2539 (truncated and full-length) being eluted around 250 mM imidazole. Protein fractions were pooled and tobacco etch virus (TEV) protease (ratio 1 : 20 (w/w)) added. The buffer was exchanged to TEV cleavage buffer D (50 mM Tris–HCl pH 7.5, 500 mM NaCl, 5% (v/v) glycerol, 1 mM DTT) in an overnight dialysis at 277 K. After incubation, the protein mixture was loaded into a 5 mL His-trap FF column (GE Healthcare) pre-equilibrated with buffer B. The mixture of protein truncated and full length was eluted with a elution step of 30% buffer C and the buffer exchanged to buffer E (50 mM Tris–HCl pH 7.5,

150 mM NaCl, 1 mM MnCl_2) using a centricon concentrator with a cutoff of 10 kDa (Millipore, Burlington, MA, USA). The sample was applied onto a Heparin column (GE Healthcare) which had previously been equilibrated with buffer E. The two forms (full-length and truncated) were separated with a linear gradient up to 100% of buffer F (50 mM Tris-HCl pH 7.5, 1 M NaCl, 1 mM MnCl_2) over 8 column volumes. The last step was a gel filtration on a Superdex 75 column (GE Healthcare) equilibrated with 50 mM Tris-HCl pH 7.5, 300 mM NaCl. The purified samples were concentrated to $10 \text{ mg} \cdot \text{mL}^{-1}$, flash-frozen in liquid nitrogen and stored at 193 K until further use.

Preparation of double-stranded DNA

Forward and reverse DNA oligonucleotides containing the different sequences designed for DNA-binding analysis and crystallisation studies were obtained from Eurofins (Table S4). To prepare double-stranded DNA, each forward and reverse oligonucleotide sample pair was resuspended in 10 mM Tris-HCl pH 7.5 and 100 mM NaCl and mixed to a final concentration of 100 μM for EMSA and 1 mM for crystallisation assays. All mixtures were then heated at 95 °C for 5 min, slowly cooled down to 56 °C for 30 min in a thermal cycler and left for 1 h at room temperature.

Crystallisation, data collection, structure solution and refinement

Initial crystallisation screenings by sitting-drop vapour diffusion method at 277 and 293 K using Greiner Crystal-Quick 96 well plates were performed with Cartesian PixSys 4200 crystallisation robot (Cartesian Technologies, Irvine, CA, USA) facility (High Throughput Crystallisation Laboratory (HTX Lab)) at EMBL Grenoble.

DR2539 truncated protein was initially screened by the following commercial crystallisation screens: Classics Suite (Qiagen, Hilden, Germany), Salt grid (Hampton Research, Hampton Research, Journey, CA, USA), Wizard I&II (Rigaku Reagents, The Woodlands, TX, USA) and JCSG + (Molecular Dimensions Limited, Calibre Scientific UK, Rotherham, UK). A cluster of needles appeared within 15 days on condition D3 from the Classics suite plate (0.1 M Hepes pH 7.5; 1 M sodium acetate; 0.05 M Cadmium sulphate) at 293 K. In order to improve crystal quality and size, the condition was scaled up to 2 μL drops with 1 : 1 protein : precipitant ratio, and precipitant concentration and pH were screened. Single crystals were obtained after 3 days in sitting drops (0.1 M Hepes pH 7.0; 1.2 M sodium acetate; 0.05 M Cadmium sulphate) and grew up to a maximum size of $0.02 \times 0.02 \times 0.4 \text{ mm}$ in 7 days. An additive screen (Hampton Research) was performed and better diffracting crystals were obtained in condition C6 (3% 6-Aminohexanoic acid; 0.1 M Hepes pH 7.0; 1.2 M sodium acetate; 0.05 M Cadmium sulphate).

To prepare the complex, Dr2539tr was incubated with *dr1709p_wt* and manganese (410, 205 and 820 μM , respectively) in 20 mM Tris-HCl pH 7.5, 150 mM NaCl. The complex was initially screened by the following commercial crystallisation screens: Nucleix (Qiagen) and Wizard I&II (Rigaku Reagents). Single crystals were obtained in condition F12 (PEG 8K 30% (w/v); Imidazole 0.1 M pH 8.0; NaCl 0.2 M) at 293 K within 24 h and diffracted up to 4 Å. The condition was scaled up to 2 μL hanging drops with 1 : 1 protein-promoter precipitant ratio, and the precipitant concentration and pH were screened. Single plates were obtained within 24 h (PEG 8K 26% (w/v); Imidazole 0.1 M pH 7.8; NaCl 0.2 M) and grew up to a maximum size of $0.05 \times 0.02 \times 0.2 \text{ mm}$ in 7 days.

Crystals were cryoprotected in mother liquor augmented with 20% (v/v) glycerol. X-ray diffraction data sets were collected at 100 K using a Pilatus 6M-F detector on ID29 [62] and ID23-1 [63] beamlines at the European Synchrotron Radiation Facility. A highly redundant anomalous dispersion data set was collected 1.771 Å on ID29 in order to obtain the maximum anomalous signal from cadmium (theoretical K-edge absorption peak at (3.085 Å)) without compromising the beam intensity. X-ray diffraction images were integrated and scaled with XDS [64]. The SHELX [65] package was used to determine the positions of the cadmium atoms and calculate initial phases. Initial model building and sequence docking was performed with ARP/wARP [66]. Finally, manual model building and interactive refinement were performed using COOT [67] and PHENIX [68], which was also used to refine the metal occupancies.

Final model was refined with a higher resolution dataset collected from a native crystal at 0.980 Å on ID23-1. X-ray diffraction data set from a crystal of DR2539 in complex with *dr1709* promoter was collected on ID29. The structure was solved by molecular replacement with Phaser [69] using the structure of DR2539 truncated obtained before as the search model. Model building and refinement were performed with COOT and PHENIX.

Small-angle X-ray scattering

Small-angle X-ray Scattering (SAXS) measurements were carried out at 293 K on beamline BM29 [70] of the ESRF at $\lambda = 0.9919 \text{ Å}$. Prior to experiments, all solutions were centrifuged at 12 000 *g* for 10 min to remove aggregated particles. Scattering data were recorded over a scattering-vector of $0.0035 < q < 0.5 \text{ Å}^{-1}$ ($q = 4\pi \sin(\theta)/\lambda$, 2θ is the scattering angle) with a Pilatus 1M detector (Dectris Ltd., Baden, Switzerland). Fifty microlitre of protein solutions were loaded into a sample capillary in flow mode and were exposed to X-ray. The scattering data were collected using multiple exposures with different times (see details in Table S5). Background buffer measurements were taken before and after every sample measurement and averaged. Data were processed and analysed with the ATSAS package

[71,72]. To obtain the zero concentration curves, the scattering curves were merged manually as described in the literature [73].

Forward scattering $I(0)$ and radius of gyration (R_g) were calculated following the Guinier approximation [74]. Particle volume and the maximum particle size (D_{max}) were calculated from the pair distribution function $P(r)$ [75] using PRIMUS [73]. Scattering curves from solutions of full-length and truncated forms were measured at different concentrations in buffer 50 mM Tris–HCl pH 7.5, 300 mM NaCl. The proteins were also dialysed in buffer supplemented with 5 mM EDTA or 5 mM $MnCl_2$. The *ab initio* shape models of DR2539 were derived from the measured scattering curve with DAMMIF [76] imposing P2 symmetry. Fifteen independently generated *ab initio* models were aligned, averaged and filtered using DAMAVER [77]. Theoretical scattering curves of DR2539 AlphaFold2 model [52], or the experimental model (PDB: 8PVZ), were calculated and fitted against experimental scattering curves using CRYSOLO [71].

Electrophoretic mobility shift assay

The electrophoretic mobility shift assays (EMSAs) were performed as previously described [16] with some modifications. 5–25 μ M of DR2539 (full-length or truncated) was incubated for 30 min at 4 °C with 1 μ M of the annealed oligos (Table S4) in EMSA binding buffer (25 mM Tris–HCl pH7.5, 150 mM NaCl, 0.5 mM $MnCl_2$ and 5% glycerol) to a final volume of 20 μ L. Different salts were tested ($MnCl_2$, $MgCl_2$, $ZnCl_2$, $(NH_4)_2Fe(SO_4)_2$, $CdSO_4$, LiCl, $NiCl_2$) at 0.5 mM and EDTA at 1 mM. After the incubation, the reaction mixtures were analysed on 5% nondenaturing (i.e. native) polyacrylamide gels. The gels were eventually incubated with SYBR green (Invitrogen) and revealed under an UV transilluminator.

Isothermal calorimetry

Isothermal calorimetry assays were conducted in triplicate at 298 K on a Microcal ITC 200 (Microcal Inc., Northampton, MA, USA) with the reference cell filled with MilliQ water. Proteins were incubated with EDTA (10 mM) in the storing buffer (25 mM Tris–HCl pH 7.5, 300 mM NaCl) and dialysed in the titration buffer (50 mM Tris–HCl pH7.5, 300 mM NaCl). Full-length and truncated forms of DR2539 at 50 μ M were titrated with 20 injections of 2 μ L of $MnCl_2$ (1.5 mM). The ORIGIN software package (Northampton, MA, USA) was used to extrapolate the integrated heat responses.

Circular dichroism measurements

Binding of DR2539 to *dr1709p* was monitored by circular dichroism (CD) spectroscopy. CD spectra (260–320 nm) were recorded at 293 K in 1-nm steps on a temperature

controlled Jasco J-815 spectropolarimeter (Tokyo, Japan), continuously purged with nitrogen gas. For each sample, the smoothed average of 16 spectra was considered. DR2539 protein was added incrementally (250, 500, 1000, 2000, 4000 nM) to a 10 mm-path quartz cuvette (500 μ L) containing *dr1709p* (2 μ M) in binding buffer (25 mM Tris–HCl pH7.5, 150 mM NaCl, 0.5 mM $MnCl_2$) and metal depletion test was performed in buffer supplemented with 2 mM EDTA.

Acknowledgements

CM acknowledges the ‘Fundação para a Ciência e Tecnologia’ (FCT) for a postdoctoral contract SFRH/BEST/51724/2011. DS and CM acknowledge Programa Pessoa from FCT and Campus France ref. 35797UH. The authors also thank the Partnership for Structural Biology, Grenoble (France) for an integrated structural biology environment and the ESRF Structural Biology Group for continuous support. Salette Reis and Claudia Pinho are gratefully acknowledged for assistance with the ITC experiments. Pedro Pereira is gratefully acknowledged for helpful discussions on the project.

Conflict of interest

The authors declare no conflict of interest.

Author contributions

CM and DdS conceived and designed all experiments and analysed all the data. CM performed all the experiments, solved and refined all structures. MW performed protein purification, biochemical characterisation and crystallisation assays. MS produced protein. UK and CZ performed molecular biology experiments and expression assays. GG performed SAXS experiments. JAM analysed SAXS data. DS supervised the project. CM and DdS wrote the manuscript with inputs from coauthors CZ, JAM and GG. All authors approved the final version of the manuscript.

Peer review

The peer review history for this article is available at <https://www.webofscience.com/api/gateway/wos/peer-review/10.1111/febs.17140>.

Data availability statement

Structural data are available in the Protein Data Bank (8PVT, 8PVZ, 8PW0).

References

- Slade D & Radman M (2011) Oxidative stress resistance in *Deinococcus radiodurans*. *Microbiol Mol Biol Rev* **75**, 133–191.
- Anderson A, Nordon H, Cain RF, Parrish G, Duggan D, Anderson A, Nordan H, Parish G & Cullum-Dugan D (1956) Studies on a radio-resistant *Micrococcus*. I. Isolation, morphology, cultural characteristics, and resistance to gamma radiation. *Food Technol* **10**, 575–577.
- Driedger AA (1970) The DNA content of single cells of *Micrococcus radiodurans*. *Can J Microbiol* **16**, 1136–1137.
- Cox MM (1999) Recombinational DNA repair in bacteria and the RecA protein. *Prog Nucleic Acid Res Mol Biol* **63**, 311–366.
- Cox MM, Goodman MF, Kreuzer KN, Sherratt DJ, Sandler SJ & Marians KJ (2000) The importance of repairing stalled replication forks. *Nature* **404**, 37–41.
- Kowalczykowski SC (2000) Initiation of genetic recombination and recombination-dependent replication. *Trends Biochem Sci* **25**, 156–165.
- Kuzminov A (2001) DNA replication meets genetic exchange: chromosomal damage and its repair by homologous recombination. *Proc Natl Acad Sci USA* **98**, 8461–8468.
- Daly MJ, Gaidamakova EK, Matrosova VY, Vasilenko A, Zhai M, Leapman RD, Lai B, Ravel B, Li S-MW, Kemner KM *et al.* (2007) Protein oxidation implicated as the primary determinant of bacterial radioresistance. *PLoS Biol* **5**, e92.
- Daly MJ (2009) A new perspective on radiation resistance based on *Deinococcus radiodurans*. *Nat Rev Microbiol* **7**, 237–245.
- Makarova KS, Aravind L, Daly MJ & Koonin EV (2000) Specific expansion of protein families in the radioresistant bacterium *Deinococcus radiodurans*. *Genetica* **108**, 25–34.
- Daly MJ, Gaidamakova EK, Matrosova VY, Kiang JG, Fukumoto R, Lee D-Y, Wehr NB, Viteri GA, Berlett BS & Levine RL (2010) Small-molecule antioxidant proteome-shields in *Deinococcus radiodurans*. *PLoS One* **5**, e12570.
- Sun H, Xu G, Zhan H, Chen H, Sun Z, Tian B & Hua Y (2010) Identification and evaluation of the role of the manganese efflux protein in *Deinococcus radiodurans*. *BMC Microbiol* **10**, 319.
- Makarova KS, Omelchenko MV, Gaidamakova EK, Matrosova VY, Vasilenko A, Zhai M, Lapidus A, Copeland A, Kim E, Land M *et al.* (2007) *Deinococcus geothermalis*: the pool of extreme radiation resistance genes shrinks. *PLoS One* **2**, e955.
- Chang S, Shu H, Li Z, Wang Y, Chen L, Hua Y & Qin G (2009) Disruption of manganese ions [Mn(II)] transporter genes DR1709 or DR2523 in extremely radio-resistant bacterium *Deinococcus radiodurans*. *Wei Sheng Wu Xue Bao* **49**, 438–444.
- Bozzi AT, Bane LB, Weihofen WA, Singharoy A, Guillen ER, Ploegh HL, Schulten K & Gaudet R (2016) Crystal structure and conformational change mechanism of a bacterial Nrap-family divalent metal transporter. *Structure* **24**, 2102–2114.
- Sun H, Li M, Xu G, Chen H, Jiao J, Tian B, Wang L & Hua Y (2012) Regulation of MntH by a dual Mn(II)- and Fe(II)-dependent transcriptional repressor (DR2539) in *Deinococcus radiodurans*. *PLoS One* **7**, e35057.
- Chen H, Wu R, Xu G, Fang X, Qiu X, Guo H, Tian B & Hua Y (2010) DR2539 is a novel DtxR-like regulator of Mn/Fe ion homeostasis and antioxidant enzyme in *Deinococcus radiodurans*. *Biochem Biophys Res Commun* **396**, 413–418.
- Santos SP, Mitchell EP, Franquelim HG, Castanho MARB, Abreu IA & Romão CV (2015) Dps from *Deinococcus radiodurans*: oligomeric forms of Dps1 with distinct cellular functions and Dps2 involved in metal storage. *FEBS J* **282**, 4307–4327.
- Chen H, Xu G, Zhao Y, Tian B, Lu H, Yu X, Xu Z, Ying N, Hu S & Hua Y (2008) A novel OxyR sensor and regulator of hydrogen peroxide stress with one cysteine residue in *Deinococcus radiodurans*. *PLoS One* **3**, e1602.
- Ul Hussain Shah AM, Zhao Y, Wang Y, Yan G, Zhang Q, Wang L, Tian B, Chen H & Hua Y (2014) A Mur regulator protein in the extremophilic bacterium *Deinococcus radiodurans*. *PLoS One* **9**, e106341.
- Haemig HAH, Moen PJ & Brooker RJ (2010) Evidence that highly conserved residues of transmembrane segment 6 of *Escherichia coli* MntH are important for transport activity. *Biochemistry* **49**, 4662–4671.
- Gunshin H, Mackenzie B, Berger UV, Gunshin Y, Romero MF, Boron WF, Nussberger S, Gollan JL & Hediger MA (1997) Cloning and characterization of a mammalian proton-coupled metal-ion transporter. *Nature* **388**, 482–488.
- Anderson ES, Paulley JT, Gaines JM, Valderas MW, Martin DW, Menscher E, Brown TD, Burns CS & Roop RM 2nd (2009) The manganese transporter MntH is a critical virulence determinant for *Brucella abortus* 2308 in experimentally infected mice. *Infect Immun* **77**, 3466–3474.
- Cellier M, Privé G, Belouchi A, Kwan T, Rodrigues V, Chia W & Gros P (1995) Nrap defines a family of membrane proteins. *Proc Natl Acad Sci USA* **92**, 10089–10093.
- Makui H, Roig E, Cole ST, Helmann JD, Gros P & Cellier MF (2000) Identification of the *Escherichia coli* K-12 Nrap orthologue (MntH) as a selective divalent metal ion transporter. *Mol Microbiol* **35**, 1065–1078.

- 26 Courville P, Chaloupka R & Cellier MFM (2006) Recent progress in structure-function analyses of Nramp proton-dependent metal-ion transporters. *Biochem Cell Biol* **84**, 960–978.
- 27 Boyd J, Oza MN & Murphy JR (1990) Molecular cloning and DNA sequence analysis of a diphtheria toxin iron-dependent regulatory element (dtxR) from *Corynebacterium diphtheriae*. *Proc Natl Acad Sci USA* **87**, 5968–5972.
- 28 Feese MD, Ingason BP, Goranson-Siekierke J, Holmes RK & Hol WG (2001) Crystal structure of the iron-dependent regulator from *Mycobacterium tuberculosis* at 2.0-Å resolution reveals the Src homology domain 3-like fold and metal binding function of the third domain. *J Biol Chem* **276**, 5959–5966.
- 29 Manabe YC, Saviola BJ, Sun L, Murphy JR & Bishai WR (1999) Attenuation of virulence in *Mycobacterium tuberculosis* expressing a constitutively active iron repressor. *Proc Natl Acad Sci USA* **96**, 12844–12848.
- 30 Yeo HK, Park YW & Lee JY (2014) Structural analysis and insight into metal-ion activation of the iron-dependent regulator from *Thermoplasma acidophilum*. *Acta Crystallogr D* **70**, 1281–1288.
- 31 Marcos-Torres FJ, Maurer D, Juniar L & Griese JJ (2021) The bacterial iron sensor IdeR recognizes its DNA targets by indirect readout. *Nucleic Acids Res* **49**, 10120–10135.
- 32 Stoll KE, Draper WE, Kliegman JI, Golynskiy MV, Brew-Appiah RAT, Phillips RK, Brown HK, Breyer WA, Jakubovics NS, Jenkinson HF *et al.* (2009) Characterization and structure of the manganese-responsive transcriptional regulator ScaR. *Biochemistry* **48**, 10308–10320.
- 33 Glasfeld A, Guedon E, Helmann JD & Brennan RG (2003) Structure of the manganese-bound manganese transport regulator of *Bacillus subtilis*. *Nat Struct Biol* **10**, 652–657.
- 34 Ando M, Manabe YC, Converse PJ, Miyazaki E, Harrison R, Murphy JR & Bishai WR (2003) Characterization of the role of the divalent metal ion-dependent transcriptional repressor MntR in the virulence of *Staphylococcus aureus*. *Infect Immun* **71**, 2584–2590.
- 35 Horsburgh MJ, Wharton SJ, Cox AG, Ingham E, Peacock S & Foster SJ (2002) MntR modulates expression of the PerR regulon and superoxide resistance in *Staphylococcus aureus* through control of manganese uptake. *Mol Microbiol* **44**, 1269–1286.
- 36 Que Q & Helmann JD (2000) Manganese homeostasis in *Bacillus subtilis* is regulated by MntR, a bifunctional regulator related to the diphtheria toxin repressor family of proteins. *Mol Microbiol* **35**, 1454–1468.
- 37 Lee MY, Lee DW, Joo HK, Jeong KH & Lee JY (2019) Structural analysis of the manganese transport regulator MntR from *Bacillus halodurans* in apo and manganese bound forms. *PLoS One* **14**, e0224689.
- 38 Cong X, Yuan Z, Wang Z, Wei B, Xu S & Wang J (2018) Crystal structures of manganese-dependent transcriptional repressor MntR (Rv2788) from *Mycobacterium tuberculosis* in apo and manganese bound forms. *Biochem Biophys Res Commun* **501**, 423–427.
- 39 Posey JE, Hardham JM, Norris SJ & Gherardini FC (1999) Characterization of a manganese-dependent regulatory protein, TroR, from *Treponema pallidum*. *Proc Natl Acad Sci USA* **96**, 10887–10892.
- 40 Olsen RJ, Sitkiewicz I, Ayeras AA, Gonulal VE, Cantu C, Beres SB, Green NM, Lei B, Humbird T, Greaver J *et al.* (2010) Decreased necrotizing fasciitis capacity caused by a single nucleotide mutation that alters a multiple gene virulence axis. *Proc Natl Acad Sci USA* **107**, 888–893.
- 41 Toukoki C, Gold KM, McIver KS & Eichenbaum Z (2010) MtsR is a dual regulator that controls virulence genes and metabolic functions in addition to metal homeostasis in the group A *Streptococcus*. *Mol Microbiol* **76**, 971–989.
- 42 Hill PJ, Cockayne A, Landers P, Morrissey JA, Sims CM & Williams P (1998) SirR, a novel iron-dependent repressor in *Staphylococcus epidermidis*. *Infect Immun* **66**, 4123–4129.
- 43 Rolerson E, Swick A, Newlon L, Palmer C, Pan Y, Keeshan B & Spatafora G (2006) The SloR/Dlg metalloregulator modulates *Streptococcus mutans* virulence gene expression. *J Bacteriol* **188**, 5033–5044.
- 44 O'Rourke KP, Shaw JD, Pesesky MW, Cook BT, Roberts SM, Bond JP & Spatafora GA (2010) Genome-wide characterization of the SloR metalloregulome in *Streptococcus mutans*. *J Bacteriol* **192**, 1433–1443.
- 45 Spatafora G, Corbett J, Cornacchione L, Daly W, Galan D, Wysota M, Tivnan P, Collins J, Nye D, Levitz T *et al.* (2015) Interactions of the metalloregulatory protein SloR from *Streptococcus mutans* with its metal ion effectors and DNA binding site. *J Bacteriol* **197**, 3601–3615.
- 46 Rangachari V, Marin V, Bienkiewicz EA, Semavina M, Guerrero L, Love JF, Murphy JR & Logan TM (2005) Sequence of ligand binding and structure change in the diphtheria toxin repressor upon activation by divalent transition metals. *Biochemistry* **44**, 5672–5682.
- 47 D'Aquino JA, Tetenbaum-Novatt J, White A, Berkovitch F & Ringe D (2005) Mechanism of metal ion activation of the diphtheria toxin repressor DtxR. *Proc Natl Acad Sci USA* **102**, 18408–18413.
- 48 D'Aquino JA, Lattimer JR, Denninger A, D'Aquino KE & Ringe D (2007) Role of the N-terminal helix in the metal ion-induced activation of the diphtheria toxin repressor DtxR. *Biochemistry* **46**, 11761–11770.

- 49 Lavery R, Moakher M, Maddocks JH, Petkeviciute D & Zakrzewska K (2009) Conformational analysis of nucleic acids revisited: curves+. *Nucleic Acids Res* **37**, 5917–5929.
- 50 Lim S, Jung J-H, Blanchard L & de Groot A (2019) Conservation and diversity of radiation and oxidative stress resistance mechanisms in *Deinococcus* species. *FEMS Microbiol Rev* **43**, 19–52.
- 51 Do H, Makthal N, Chandrangu P, Olsen RJ, Helmann JD, Musser JM & Kumaraswami M (2019) Metal sensing and regulation of adaptive responses to manganese limitation by MtsR is critical for group A *Streptococcus* virulence. *Nucleic Acids Res* **47**, 7476–7493.
- 52 Jumper J, Evans R, Pritzel A, Green T, Figurnov M, Ronneberger O, Tunyasuvunakool K, Bates R, Židek A, Potapenko A *et al.* (2021) Highly accurate protein structure prediction with AlphaFold. *Nature* **596**, 583–589.
- 53 Chakrabarti P (1990) Geometry of interaction of metal ions with histidine residues in protein structures. *Protein Eng* **4**, 57–63.
- 54 Love JF, van der Spek JC, Marin V, Guerrero L, Logan TM & Murphy JR (2004) Genetic and biophysical studies of diphtheria toxin repressor (DtxR) and the hyperactive mutant DtxR(E175K) support a multistep model of activation. *Proc Natl Acad Sci USA* **101**, 2506–2511.
- 55 Wisedchaisri G, Holmes RK & Hol WGJ (2004) Crystal structure of an IdeR-DNA complex reveals a conformational change in activated IdeR for base-specific interactions. *J Mol Biol* **342**, 1155–1169.
- 56 Lee JH, Wang T, Ault K, Liu J, Schmitt MP & Holmes RK (1997) Identification and characterization of three new promoter/operators from *Corynebacterium diphtheriae* that are regulated by the diphtheria toxin repressor (DtxR) and iron. *Infect Immun* **65**, 4273–4280.
- 57 Pohl E, Holmes RK & Hol WG (1999) Crystal structure of a cobalt-activated diphtheria toxin repressor-DNA complex reveals a metal-binding SH3-like domain. *J Mol Biol* **292**, 653–667.
- 58 Pohl E, Holmes RK & Hol WG (1998) Motion of the DNA-binding domain with respect to the core of the diphtheria toxin repressor (DtxR) revealed in the crystal structures of apo- and holo-DtxR. *J Biol Chem* **273**, 22420–22427.
- 59 Qiu X, Pohl E, Holmes RK & Hol WG (1996) High-resolution structure of the diphtheria toxin repressor complexed with cobalt and manganese reveals an SH3-like third domain and suggests a possible role of phosphate as co-corepressor. *Biochemistry* **35**, 12292–12302.
- 60 Stevenson B, Wyckoff EE & Payne SM (2016) *Vibrio cholerae* FeoA, FeoB, and FeoC interact to form a complex. *J Bacteriol* **198**, 1160–1170.
- 61 Marcos-Torres FJ, Juniar L & Griesse JJ (2023) The molecular mechanisms of the bacterial iron sensor IdeR. *Biochem Soc Trans* **51**, 1319–1329.
- 62 de Sanctis D, Beteva A, Caserotto H, Dobias F, Gabadinho J, Giraud T, Gobbo A, Guijarro M, Lentini M, Lavault B *et al.* (2012) ID29: a high-intensity highly automated ESRF beamline for macromolecular crystallography experiments exploiting anomalous scattering. *J Synchrotron Radiat* **19**, 455–461.
- 63 Nurizzo D, Mairs T, Guijarro M, Rey V, Meyer J, Fajardo P, Chavanne J, Biasci JC, McSweeney S & Mitchell E (2006) The ID23-1 structural biology beamline at the ESRF. *J Synchrotron Radiat* **13**, 227–238.
- 64 Kabsch W (2010) XDS. *Acta Crystallogr D* **66**, 125–132.
- 65 Sheldrick GM (2008) A short history of SHELX. *Acta Crystallogr A* **64**, 112–122.
- 66 Morris RJ, Perrakis A & Lamzin VS (2003) ARP/wARP and automatic interpretation of protein electron density maps. *Methods Enzymol* **374**, 229–244.
- 67 Emsley P & Cowtan K (2004) Coot: model-building tools for molecular graphics. *Acta Crystallogr D* **60**, 2126–2132.
- 68 Adams PD, Afonine PV, Bunkóczi G, Chen VB, Davis IW, Echols N, Headd JJ, Hung L-W, Kapral GJ, Grosse-Kunstleve RW *et al.* (2010) PHENIX: a comprehensive Python-based system for macromolecular structure solution. *Acta Crystallogr D* **66**, 213–221.
- 69 McCoy AJ, Grosse-Kunstleve RW, Adams PD, Winn MD, Storoni LC & Read RJ (2007) Phaser crystallographic software. *J Appl Cryst* **40**, 658–674.
- 70 Pernot P, Round A, Barrett R, De Maria Antolinos A, Gobbo A, Gordon E, Huet J, Kieffer J, Lentini M, Mattenet M *et al.* (2013) Upgraded ESRF BM29 beamline for SAXS on macromolecules in solution. *J Synchrotron Radiat* **20**, 660–664.
- 71 Franke D, Petoukhov MV, Konarev PV, Panjkovich A, Tuukkanen A, Mertens HDT, Kikhney AG, Hajizadeh NR, Franklin JM, Jeffries CM *et al.* (2017) ATSAS 2.8: a comprehensive data analysis suite for small-angle scattering from macromolecular solutions. *J Appl Cryst* **50**, 1212–1225.
- 72 Petoukhov MV, Franke D, Shkumatov AV, Tria G, Kikhney AG, Gajda M, Gorba C, Mertens HDT, Konarev PV & Svergun DI (2012) New developments in the ATSAS program package for small-angle scattering data analysis. *J Appl Cryst* **45**, 342–350.
- 73 Manalastas-Cantos K, Konarev PV, Hajizadeh NR, Kikhney AG, Petoukhov MV, Molodenskiy DS, Panjkovich A, Mertens HDT, Gruzinov A, Borges C *et al.* (2021) ATSAS 3.0: expanded functionality and new tools for small-angle scattering data analysis. *J Appl Cryst* **54**, 343–355.

- 74 Guinier A & Fournet G (1955) Small-Angle Scattering of X-Rays. Wiley, New York, NY.
- 75 Svergun DI (1992) Determination of the regularization parameter in indirect-transform methods using perceptual criteria. *J Appl Cryst* **25**, 495–503.
- 76 Franke D & Svergun DI (2009) DAMMIF, a program for rapid ab-initio shape determination in small-angle scattering. *J Appl Cryst* **42**, 342–346.
- 77 Volkov VV & Svergun DI (2003) Uniqueness of ab initio shape determination in small-angle scattering. *J Appl Cryst* **36**, 860–864.
- 78 Schrödinger, LLC (2015) The PyMOL Molecular Graphics System, Version 3.0.
- 79 Luscombe NM, Laskowski RA & Thornton JM (1997) NUCPLOT: a program to generate schematic diagrams of protein-nucleic acid interactions. *Nucleic Acids Res* **25**, 4940–4945.

Supporting information

Additional supporting information may be found online in the Supporting Information section at the end of the article.

Fig. S1. HiTrap Heparin HP affinity chromatography profile separation of truncated and full-length forms of DR2539.

Fig. S2. Sequence alignment of *D. radiodurans* DR2539 and representatives of DtxR/MntR family.

Fig. S3. Superdex S75 elution profile of DR2539.

Fig. S4. DNA maps ambiguity.

Fig. S5. Major and minor grooves parameters calculated by Curves+ for *dr1709p* and ideal B-DNA.

Fig. S6. Binding of DR2539 to *dr1709p* was monitored by circular dichroism (CD) spectroscopy.

Fig. S7. Model of DR2539 determined by AlphaFold2.

Fig. S8. Small-angle X-ray scattering (SAXS) of DR2539 full-length and truncated.

Fig. S9. Comparison of the experimental scattering curves of truncated DR2539 as isolated, incubated with EDTA or manganese.

Fig. S10. Phylogenetic tree. Comparison of DBDs sequences from the DtxR family members.

Table S1. Dimer interface of DR2539 truncated form.

Table S2. Cadmium atoms in structure 8PVZ.

Table S3. Protein-DNA interface.

Table S4. Oligonucleotides sequences of the *dr1709* promoter region and variants used for crystallisation and EMSA assays.

Table S5. Small-angle X-ray scattering data collection and processing.